Soft Matter

PAPER

View Article Online
View Journal | View Issue

Cite this: *Soft Matter*, 2019, 15, 4890

Distortion-controlled isotropic swelling: numerical study of free boundary swelling patterns

Carlos M. Duque, Bryan Gin-ge Chen and Christian D. Santangelo*

Received 22nd February 2019,
Accepted 23rd May 2019

DOI: 10.1039/c9sm00392d

rsc.li/soft-matter-journal

Modern fabrication tools have now provided a number of platforms for designing flat sheets that, by virtue of their nonuniform growth, can buckle and fold into target three-dimensional structures. Theoretically, there is an infinitude of growth patterns that can produce the same shape, yet almost nothing is understood about which of these many growth patterns is optimal from the point of view of experiment, and few can even be realized at all. Here, we ask the question: what is the optimal way to design isotropic growth patterns for a given target shape? We propose a computational algorithm to produce optimal growth patterns by introducing cuts into the target surfaces. Within this framework, we propose that the patterns requiring the fewest or shortest cuts produce the best approximations to the target shape at finite thickness. The results are tested by simulation on spherical surfaces, and new challenges are highlighted for surfaces with both positive and negative Gaussian curvatures.

Shape-morphing materials have been proposed as an advanced manufacturing tool to produce three-dimensional geometries from initially flat substrates. The idea of dubbed "4D printing"[1] is that materials are patterned to grow non-uniformly upon exposure to some stimulus, and the strains induced by this growth are alleviated by buckling into precise three-dimensional target shapes. This patterning can be achieved by manipulating the composition of a polymer gel,[2–4] the deposition of fibers,[5] or the configuration of nematic order parameters.[6–8] Nature demonstrates what could be achieved: buckling due to non-uniform strains have been implicated in the shaping of bacterial films,[9] the blooming of flowers[10] and the shaping of organs.[11]

Yet, all materials have limitations, whether it is a limited range of growth or a limited pattern resolution. As an example, consider the hydrogel system of Na *et al.*,[4] in which the local crosslink density of a polymer film can be programmed. When swelled with water, regions of high crosslink density swell less than those with lower crosslink density, leading to buckling into three dimensions. This growth is bounded however: areas can grow anywhere from two to six times but not more (or less). In light of these limitations, one major obstacle to adopting 4D printing more broadly is the lack of understanding of the broader principles behind how growth patterns should be designed around these physical limitations.

In this paper, we ask the following question: how do we design the optimal shape of an initially flat domain and a local pattern of isotropic growth in order to produce a specific target shape? To answer this question, we first formulate an optimization problem for growth that can be applied to arbitrarily shaped surfaces with a disk topology. We then introduce the notion of cutting the surface and find that the swelling range can be reduced significantly further, albeit at the expense of a thickness-dependent fidelity.

Department of Physics, University of Massachusetts, Amherst, MA 01003, USA. E-mail: csantang@physics.umass.edu

1 Formulation and methods

1.1 Optimal, isotropic growth

We assume that a small patch of area located at point $\mathbf{x}$ in the initial flat domain grows by a factor of $\Omega(\mathbf{x}) = e^{u(\mathbf{x})}$. In the limit of zero thickness, the relationship between the target shape and the initial flat domain is given by a conformal map which takes infinitesimal circles on the initial domain to circles on the target shape.[12,13] Consequently, the Gaussian curvature at the point on the buckled sheet convected from $\mathbf{x}$, which we denote $K(\mathbf{x})$, is given by Gauss's theorema egregium,

$$2K(\mathbf{x})e^{u(\mathbf{x})} = -\nabla^2 u(\mathbf{x}). \quad (1)$$

For surfaces of constant Gaussian curvature, $K(\mathbf{x}) = K$, the previous equation reduces to the Liouville equation, which admits a general solution in terms of some meromorphic function $f(z)$ satisfying $f'(z) \neq 0$ in its domain of definition.[14]

Our basic procedure is outlined schematically in Fig. 1. We start with a target shape with a single boundary which, in principle, may penetrate into the bulk of the shape in the form of a long cut. We then fix $K(\mathbf{x})$ on the target surface and use eqn (1) to solve for $u(\mathbf{x})$.[2] Thus, if we proceed to shrink the target surface according to the areal distortion $\Omega^{-1} = \exp[-u(\mathbf{x})]$, we would obtain a flat domain. Mathematically, the map connecting the final shape to the target shape itself is determined uniquely

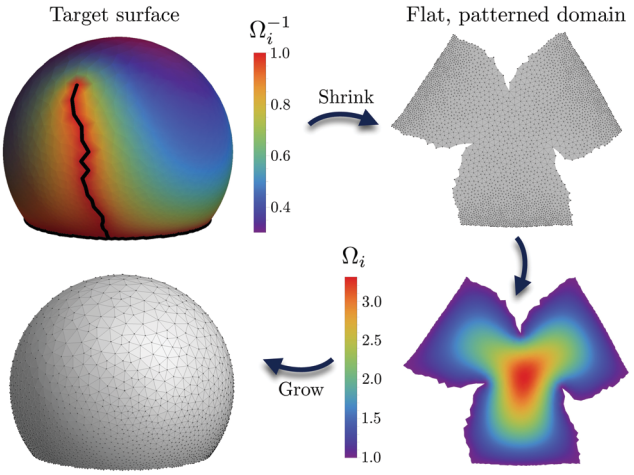

Fig. 1 A target surface (with some additional cuts) can be deswelled to a flat domain. The inverse swelling map can be used to recover the target surface. The surfaces are colored with respect to the conformal factor per vertex Ω_i.

from a single harmonic function on the target surface mapping the boundary of the flat domain to the boundary of the target shape.[15] Finally, this flat domain, when subjected to nonuniform growth by the areal distortion $\Omega(\mathbf{x}) = \exp[u(\mathbf{x})]$ will, at least in principle, reproduce the target surface in the limit of zero thickness.[13] Yet, there are an infinite number of maps between the target shape and a flat, disk-like domain depending on how we choose the boundary and the boundary conditions for $u(\mathbf{x})$ on the target shape; any one of these solutions would be a pattern of growth that, in theory, was guaranteed to produce the same target surface in the limit of zero thickness.

Thus, we require a criterion that allows us to determine both the ideal boundary and the appropriate boundary conditions on $u(\mathbf{x})$. To do so, we consider two measures of the range of growth in a given pattern of growth. The Chebyshev measure, $\omega_C \equiv \ln(\Omega_{max}/\Omega_{min})$, where Ω_{min} and Ω_{max} are the smallest and largest growth factors, respectively, is the most natural experimentally. For example, in any experimental realization, we require ω_C to be smaller than a critical value. As a second quantity, we consider the Dirichlet measure,

$$\omega_D = \frac{1}{2}\int d^2x[\nabla u(\mathbf{x})]^2, \tag{2}$$

which penalizes gradients of growth.

If the actual boundary shape of the target surface is fixed, it can be shown that the extrema of the Dirichlet measure always have $u(\mathbf{x})$ constant on the boundary.[16] Thus, it only remains to identify an appropriate boundary shape on the target surface. For ω_C, less is known, however. It was first conjectured by Chebyshev and proven by Gravé[17–19] that, so long as the Gaussian curvature does not change sign, the optimal $\Omega(\mathbf{x})$ will be constant on the boundary and take on either its maximum or minimum value depending on the sign of K. Thus, when $K > 0$ (or $K < 0$), the solutions to both optimization problems are the same; on surfaces with both positive and negative Gaussian curvatures, however, there is neither a requirement that they lead to the same solution nor that the Chebyshev measure is even well-defined on surfaces with both signs of Gaussian curvature.

It is also possible to use different energy measures. Sharp *et al.*[20] also consider a modified version of the Dirichlet energy $\omega_D^{mod} = \frac{1}{2}\int d^2x a(\mathbf{x})[\nabla u(\mathbf{x})]^2$ that uses the function $a(\mathbf{x})$ to penalize distortion non-uniformly. Additionally, the energy $\omega_H = \frac{1}{2}\int d^2x u(\mathbf{x})^2$, called the Hencky energy, which makes use of the material strain $u(\mathbf{x})$ can be used as a distortion measure. Nonetheless, it is still necessary to determine the appropriate boundary conditions for $u(\mathbf{x})$ that minimize these measures and whether or not the resulting mapping is unique as in the case of the Chebyshev and standard Dirichlet measures. In what follows, we call any conformal projection with $u(\mathbf{x})$ constant on the boundary a Chebyshev map, and we explicitly set $u(\mathbf{x}) = 0$ on the boundary. Under this boundary condition, the length of the boundary, including cuts, remains constant. We lose no generality by doing this, however, since an overall shift of $u(\mathbf{x}) = u(\mathbf{x}) + u_0$ can be absorbed into a rescaling of the Gaussian curvature, $K(\mathbf{x}) \to e^{-u_0}K(\mathbf{x})$, without changing ω_C or ω_D.

1.2 Discrete conformal maps

In order to produce a discrete representation of a conformal map, we imagine that both our target surface and initial flat domain have been decorated with the same random triangulation, created by randomly flipping the internal edges of a hexagonal triangulation. The triangulation T is characterized by V vertices joined by E edges and spanned by F faces. We label the vertices with an integer i, and define a function, u_i, on the vertices. If the vertices i and j are connected by an edge, we define the length of the edge as l_{ij}. One can then define a discretized version of conformal equivalence using[16]

$$\tilde{l}_{ij} = e^{(u_i+u_j)/4}l_{ij}. \tag{3}$$

The discrete equivalent of the Gaussian curvature for interior and boundary vertices i is given by the angle deficit:[16]

$$K_i = \begin{cases} 2\pi - \sum_n \Delta\theta_{i,n}, & \text{in } T, \\ \pi - \sum_n \Delta\theta_{i,n}, & \text{at } \partial T. \end{cases} \tag{4}$$

The angles $\Delta\theta_{i,n}$ can be determined entirely from the lengths l_{ij} of the flat triangulation through the law of cosines. Solving this non-linear system of equations accounts for finding a discrete conformal flattening of the surface of interest. We then set $u_i = 0$ on the boundary vertices. Every internal vertex of the triangulation then determines a nonlinear equation for u_i by setting $K_i = 0$ on each internal vertex of the triangulation. This gives us an alternate set of edge lengths from which we can determine new embedding of the triangulation in the plane. The resulting map from the triangulation on the curved surface to the triangulation on the conformally flat domain is a discrete conformal map, and is determined uniquely for a given boundary.[16]

We build up cuts to the surface by sequentially separating pairs of adjacent faces so that they are no longer constrained to share edges, which we call slits for clarity (Fig. 2). Thus, each

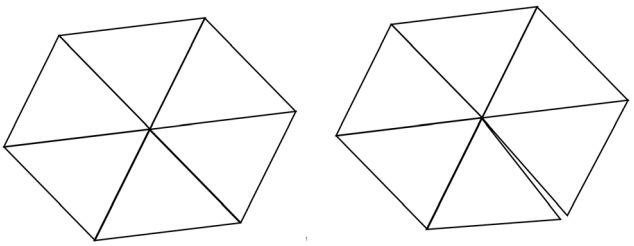

Fig. 2 A schematic of how a slit separates one triangular face from another. A longer cut is built from a sequence of slits.

cut is a concatenation of individual slits connected to the original boundary of the domain (details in Appendix A.2).

The Chebyshev measure, ω_C, generalizes naturally to the discrete case. For the Dirichlet measure, ω_D, we use the discretized form:[21]

$$\omega_D = \frac{1}{2}\sum_{\langle i,j\rangle} w_{ij}(u_i - u_j)^2, \tag{5}$$

where

$$w_{ij} = \begin{cases} (\cot\alpha_{ij} + \cot\beta_{ij})/2, & \text{for interior edges,} \\ \cot\alpha_{ij}/2, & \text{for boundary edges.} \end{cases} \tag{6}$$

Here α_{ij} and β_{ij} are the opposite angles of the interior edge l_{ij} and similarly for boundary edges which only have one opposite angle. Notice that since $u_i = 0$ for all boundary vertices, we only need to sum over the interior edges in eqn (5).

At each step in the algorithm, we create a slit with one vertex on the boundary of the domain on the edge that reduces either ω_C or ω_D the most. In this paper we mainly focus on minimizing ω_C since we expect equivalent results to the Dirichlet measure ω_D for surfaces with fixed Gaussian curvature sign. We minimize with respect to ω_D when we relax the fixed sign constraint (see Appendix A.2). Because this is a greedy algorithm, once a cut is formed, further slits tend to extend the length of a cut. However, if we seed the edges with one or more initial slits, all of the subsequent cuts appear to grow uniformly fast. Fig. 1 shows a conformal projection from an almost-complete sphere of radius R and area $A_{SC} = (4/5)A_{sph}$ in which a disk around the south pole has been removed. In the figure, three cuts have been introduced into the surface so that, after flattening, the resulting domain has three lobes.

There could be different optimal cutting techniques producing similar or better results. For example, Sharp *et al.*[20] considered a non-greedy variational approach that decreases the area distortion while penalizing the cutting length. In this case, however, the authors focus on finding the cuts on the smooth formulation rather than along the edges of some precomputed discretization. Additionally the main focus of their exposition is to partition a given surface into two or more subregions. Our algorithm can be seen as the special case where disconnected regions of low distortion are forbidden since in those cases the resulting discrete conformal parameterizations cannot be realized by swelling experiments.

As we will see, cutting driven by ω_C and ω_D primarily produces the same results so long as K has one sign. On mixed or more complex surfaces, however, there can be differences.

1.3 Simulations of surface growth

In order to test the maps produced, we performed simulations of a growing elastic sheet using a modified version of the Seung–Nelson model.[22] We triangulate the initial flat domain, label the vertices with an integer, and assign a length $\tilde{l}_{ij}$ to each edge joining vertex i to vertex j. Denoting the position of vertex i by $\mathbf{X}_i$, we assume each edge has an elastic energy

$$E_{\text{elastic}} = \frac{1}{2}\left[(\mathbf{X}_i - \mathbf{X}_j)^2 - \tilde{l}_{ij}^2\right]^2. \tag{7}$$

To incorporate bending energy, if two faces, I and J, are joined by an edge, then we add a term

$$E_{\text{bending}} = \frac{1}{2}t^2(\hat{\mathbf{n}}_I - \hat{\mathbf{n}}_J)^2, \tag{8}$$

where t is the effective elastic thickness of the sheet and $\hat{\mathbf{n}}_I$ is the unit normal vector of face I. Also note that the two energy contributions are normalized by the elastic thickness t. We minimize the energy $E_{\text{elastic}} + E_{\text{bending}}$ with respect to the vertex positions, $\mathbf{X}_i$, using a BFGS minimization algorithm or conjugate gradient algorithm provided in Mathematica, using a previously published protocol[23] to avoid "mis-folds" and non-smooth shapes using the metric

$$\tilde{l}_{ij}(\alpha) = \alpha l_{ij}^{\text{target}} + (1 - \alpha)\, l_{ij}^{\text{initial}}. \tag{9}$$

Take α from slightly above 0 on an initial domain with a small (less than 1%) curvature to bias the initial buckling to 1 on the final target surface. We can tune the thickness t in order to make it much smaller compared to any other relevant spatial dimensions. This ensures that we are in an elastic energy regime where the stretching component dominates over bending and nearly isometric deformations are preferred.

2 Results

2.1 Optimal growth patterns for spheres

We start by generating cut patterns on the sphere of radius R_{sph} shown in Fig. 1. In order to have a more local view of the area distortion we define the distortion per vertex as $\omega_{C,i} = \log(\Omega_i/\Omega_{\min})$ and always normalize it with respect to $\omega_C^{(0)} = \log(\Omega_{\max}^{(0)}/\Omega_{\min})$, where $\Omega_{\max}^{(0)}$ corresponds to the largest swelling change of the uncut or reference domain. When no cuts are present, our numerics reproduce stereographic projection of the sphere to a disk in the plane, a pattern that is known to reproduce a spherical shape at small thickness.[2,3] Also note that as was shown by Milnor,[19] there are some rough estimates of the distortion introduced by projections (not necessarily conformal) from the sphere to the plane. One way this can be done is by enclosing the spherical surface between two semicircles. The angle, $\alpha < \pi$, at the intersection of the two semicircles can be used to estimate the distortion $\omega \geq \omega_C$ as $\omega = \log\sec(\alpha/2)$. Nevertheless, this angle is not a useful estimate of the distortion of cut domains since it is not sensitive to the boundary changes introduced by the cuts which are expected to greatly reduce the flattening distortion. Typical results for the optimal shapes of 3 and 6 cuts and the associated growth patterns are shown in Fig. 3. As expected in the case of positive Gaussian curvature, cutting to minimize the Chebyshev

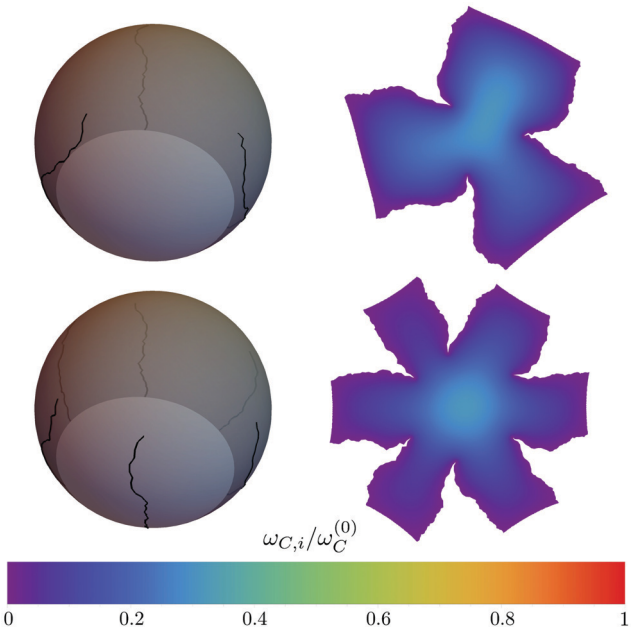

Fig. 3 Cut paths on the spherical surface (left) and planar projections (right) after using the minimum area distortion boundary conditions. We consider 3 (top) and 6 (bottom) independent cuts on surface triangulations of nearly 10 000 vertices. In both cases we stopped cutting at $\omega_C \approx 0.91$ and normalized with $\omega_C^{(0)} \approx 3.18$.

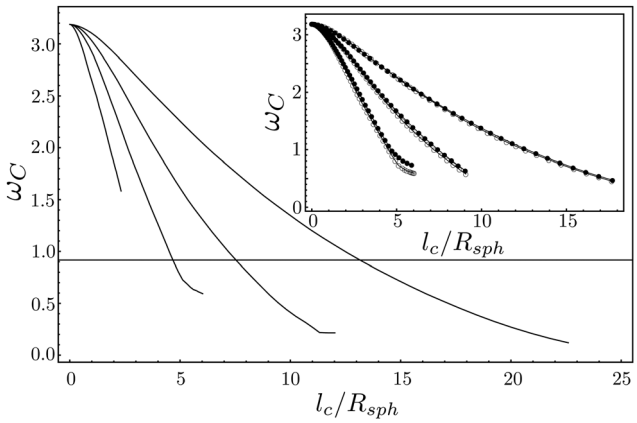

Fig. 4 Swelling ratio ω_C as a function of the cut length l_c normalized to the spherical radius R_{sph}. We show the results for 1, 3, 6 and 12 radial cuts from left to right. In the inset we show the results for 3, 6 and 12 independent cuts (●) and compare them with their radial counterparts (○) from left to right. The horizontal line corresponds to the target area distortion $\omega_C = \log(2.5) = 0.91$.

measure and Dirichlet measure produce the same results: one or more radial cuts. In both cases, the Chebyshev measure, $\omega_C = \ln(\Omega_{max}/\Omega_{min})$, decreases rapidly as the cuts penetrate further into the sphere until it reaches a plateau (Fig. 4). In addition, we checked that, if we measure cut length l_c in units of the sphere radius R_{sph}, the data using different triangulations and different numbers of vertices collapse (not shown). Based on these numerical results, we expect that the true optimal cut shape is purely radial and that the meandering is numerical noise. Indeed, when we compare ω_C of the optimal cuts from the greedy algorithm to ω_C of purely radial cuts along the lines of longitude of the sphere, we find excellent agreement, with the radial cuts having a slightly lower ω_C for the same length of cuts (inset of Fig. 4).

If we allow each independent cut to have a length larger than one full radial length, the algorithm eventually adds slits to the initial surface in a somewhat disordered fashion. This behavior is characterized by the tendency of the growing cut to constantly branch. As this happens, we observe that both ω_C and ω_D reach a plateau (not shown). The increasing cut length, as we approach ratios $\omega_C \approx 0$, makes the generated patterns of little to null usage given the boundary layers developed on patterns with an overly extended boundary. This suggests that a better strategy comes from choosing the minimum number of independent cuts that allow us to reach the desired distortion while avoiding the unwanted plateau regime. In the case of the spherical surface we are considering, this will depend on the covered surface area.

To see how the resulting patterns with different numbers of cuts perform in reproducing the original spherical shape at finite thickness, we performed simulations using the modified Nelson–Seung model described in Section 1.3. We see that we are able to recover the original sphere upon swelling the optimal domains at small thicknesses precisely as expected. We use the integrated Gaussian curvature and the integrated mean curvature squared as two independent ways of calculating the fidelity of our shapes after swelling. The Gaussian curvature in the spherical case, $K = 1/R_{sph}^2$, is constant and equal to the mean curvature squared. Thus, both integrated measures produce the same result. In general, given their intrinsic and extrinsic origins, these two shape measures should be considered independently. In Fig. 5, we plot the normalized total Gaussian curvature of the swelled and buckled domains for 1, 2, 3, and 6 cuts at fixed $\omega_C \approx 1.17$. We note that fewer cuts result in a better approximation to the original sphere given that the normalized integrated Gaussian curvature is closer to its ideal value of 1 as we vary the thickness. We can rationalize this behavior by noting that the total length of boundary is itself shorter with fewer cuts.

2.2 Surfaces with non-constant Gaussian curvature

We next look at surfaces with varying Gaussian curvature. In Fig. 6, we consider half of an ellipsoid satisfying the equation $x^2/a^2 + y^2/b^2 + z^2/z^2$, with $a = 2.5$ and $b = c = 1$. This surface has $K > 0$ everywhere and is given by:

$$K = \frac{(abc)^2}{\left[(ab\cos\theta)^2 + c^2(a^2\sin^2\phi + b^2\cos^2\phi)\sin^2\theta\right]}, \qquad (10)$$

where $\phi \in [0,2\pi)$ and $\theta \in [0,\pi]$. When the cuts are not seeded on the boundary, they naturally emerge at either of the two poles and rapidly move toward the closest maximum of Ω in the absence of any cuts. In order to produce patterns with two cuts, we seed initial cuts at both poles simultaneously and find that the cuts subsequently grow symmetrically.

Both ellipsoids in Fig. 6 are cut until ω_C reaches the same, fixed factor ($\omega_C \approx 0.24$). Unlike the case of the sphere, the ellipsoid with two cuts has a shorter boundary than the ellipsoid with one cut; as might then be expected, the surface with two cuts better reproduces the original ellipsoidal shape upon growth (Fig. 7 and 10). Indeed, the ellipsoid with a single long cut never manages to

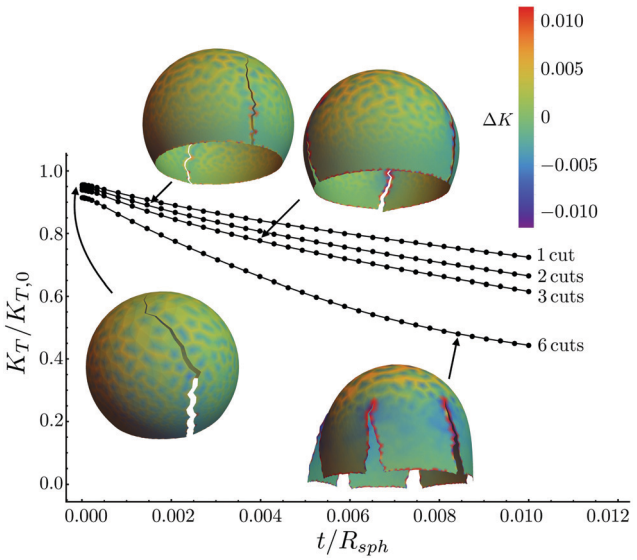

Fig. 5 Normalized total Gaussian curvature of a sphere with 1, 2, 3 or 6 cuts as a function of thickness t/R_{sph}. In all cases $\omega_C \approx 1.17$.

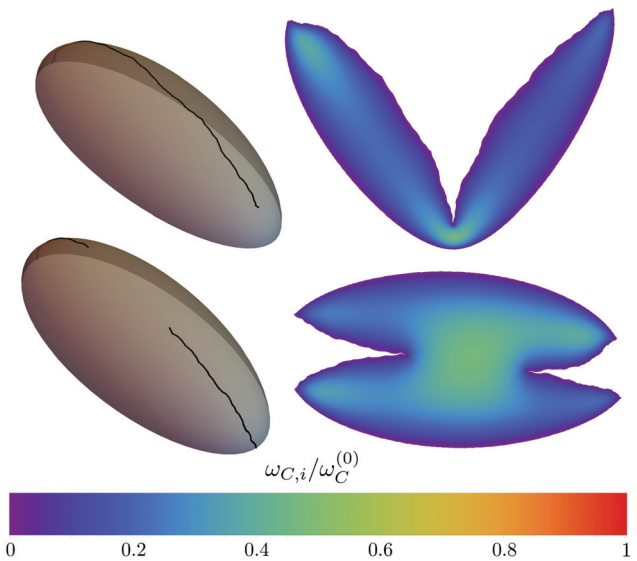

Fig. 6 Cut paths on an ellipsoidal surface (left) and optimal projections (right) for 1 (top) and 2 (bottom) independent cuts. We use the same number of vertices as in Fig. 3 and we stopped cutting right after $\omega_C \approx 0.24$ and $\omega_C^{(0)} \approx 0.54$ in both cases.

close, and its total Gaussian curvature is about 20% of the initial shape even for the thinnest structures we were able to produce.

For a prototypical surface with both signs of Gaussian curvature, we consider a Gaussian bump described by the height function $z(r) = z_0 \exp(-r^2/2R^2)$ with Gaussian curvature:[24]

$$K = \frac{\alpha^2 e^{-r'^2}}{R^2} \frac{1 - r'^2}{\left(1 + \alpha^2 r'^2 e^{-r'^2}\right)^2}, \quad (11)$$

where $r' = r/R$ and $\alpha = z_0/R$. The Gaussian curvature is positive, zero, and negative for $r < R$, $r = R$, and $r > R$ respectively.

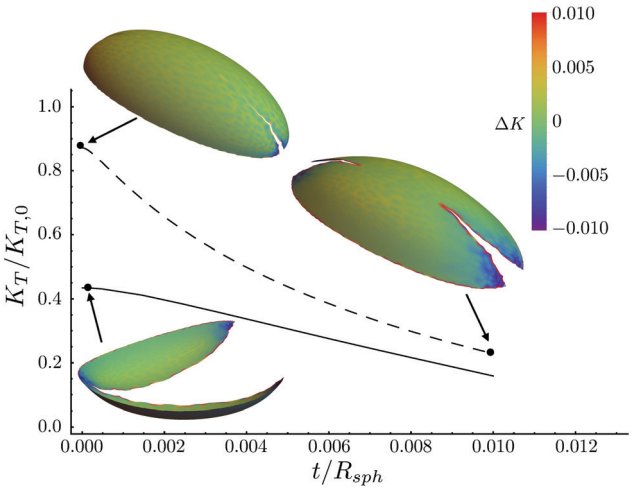

Fig. 7 Thickness dependence of the normalized total Gaussian curvature of half an ellipsoid with 1 (solid) or 2 (dashed) cuts. In both cases $\omega_C \approx 0.23$.

Without cuts, the conformal projection with Ω constant on the boundary can be written in terms of coordinates (ρ,θ) with metric $ds^2 = \Omega(\rho)(d\rho^2 + \rho^2 d\theta^2)$. The swelling factor $\Omega(\rho)$, after some work, can be shown to satisfy the first order equation (additional details in Appendix A.1):

$$\frac{1}{2\Omega(\rho)\rho}\frac{d}{d\rho}\left(\Omega(\rho)\rho^2\right) = \left[1 + \frac{z_0^2\rho^2}{R^4}\Omega(\rho)e^{-\Omega(\rho)\rho^2/R^2}\right]^{-1/2}. \quad (12)$$

Notice that the right-hand side of eqn (12) is always less than 1. This implies that

$$\frac{\Omega'(\rho)\rho}{2\Omega(\rho)} + 1 \leq 1, \quad (13)$$

or that $\Omega'(\rho) \leq 0$. Thus, we see that the Gaussian bump, while not having strictly positive Gaussian curvature, nevertheless satisfies the property that $\Omega(\rho)$ on the boundary is a minimum value. Note, however, that once cuts are introduced, there is no longer a guarantee that the minimum value of Ω occurs on the boundary.

In Fig. 8, we show the results of applying our algorithm to the Gaussian bump by choosing slits to minimize the Dirichlet energy and introducing slits that minimize the Chebyshev parameter ω_C. Only once the cutting procedure has reached the plateau regime and the introduction of slits proceeds in a seemingly random fashion; do we see any deviation between these two cases. If we choose ω_C before the plateau regime, we are able to recover the original Gaussian bump shape in both the cases of one and three cuts upon swelling (Fig. 9 and 10). The fidelity of the finite-thickness shape using the one-cut pattern, which has a shorter boundary than the three-cut pattern, appears to be better as a function of thickness.

It is worth mentioning that the branched cuts are consistent across geometries, discretizations, and levels of refinement. It seems that once the cuts reach the vicinity of an interior maximum, new highly delocalized maxima emerge and the cutting paths branch in order to account for the new maxima. The presence of branches appears to be a clear indication of the viability and limits of a greedy strategy on overly cut surfaces.

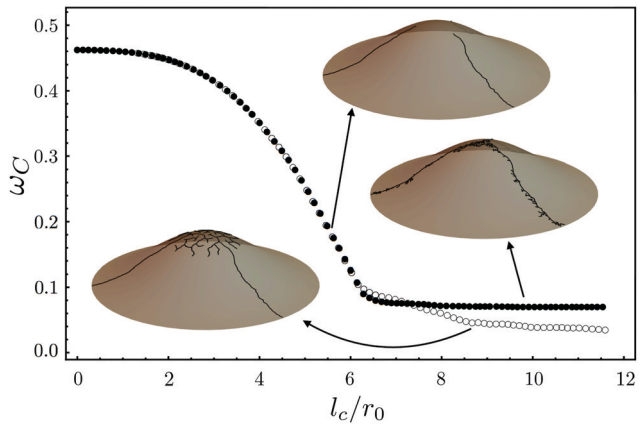

Fig. 8 Cut-length dependent ω_C for Chebyshev (●) and Dirichlet (○)energy driven cuts for a Gaussian bump surface. We consider 3 independent cuts. The inset figures highlight the common regime and the branching regimes for the 2 different cutting methods.

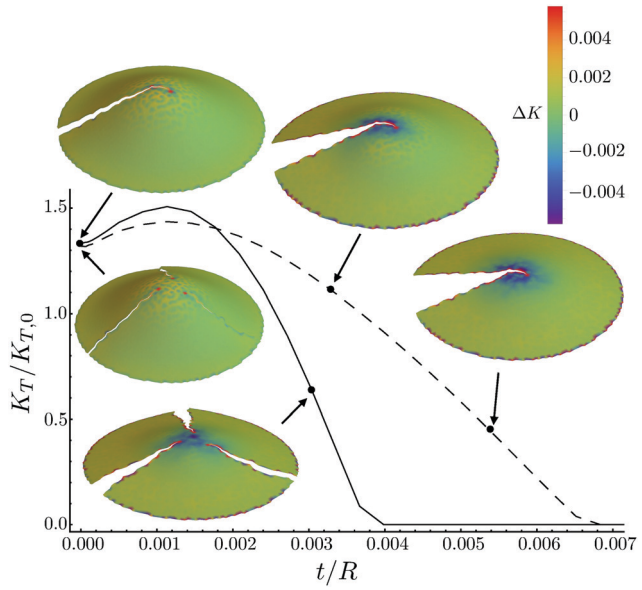

Fig. 9 Thickness dependence of the normalized total Gaussian curvature of a bump with 1 (dashed) and 3 (solid) cuts. We use $z_0 = R = 1$. In both cases $\omega_C \approx 0.13$.

Finally, we note that our procedure does not produce viable results on more general surfaces with mixed positive and negative Gaussian curvatures. Consider, for example, the undulated surface shown in Fig. 11. Without cuts, the conformal map that minimizes the Dirichlet energy (and has constant Ω on the boundary) also has many minima and maxima in Ω within the domain. In this case, the two cutting procedures deviate quickly and the resulting cuts are once again highly branched.

3 Conclusions

To conclude, we have shown how different kinds of cutting paths can be used to lower the distortion associated with the swelling

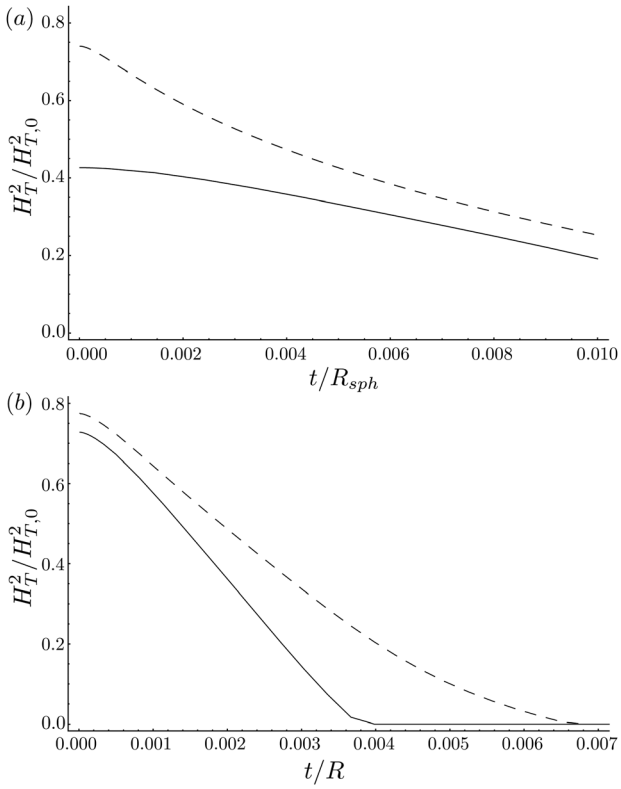

Fig. 10 (a) Thickness dependence of the normalized total mean curvature squared for the ellipsoidal surface (Fig. 7). We considered 1 (solid) and 2 (dashed) cuts. (b) Analogue calculation for the Gaussian bump (Fig. 9) with 1 (dashed) and 3 (solid) cuts.

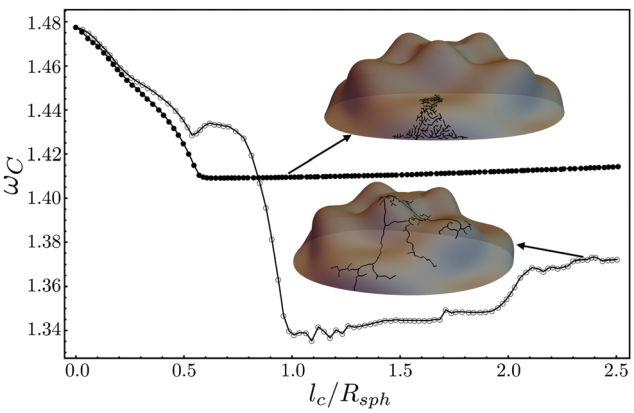

Fig. 11 Cut-length dependent ω_C for Chebyshev (●) and Dirichlet (○) energy driven cuts for an undulating sphere. We show results for a single cut and use the insets to demonstrate the cutting paths for both methods.

of elastic sheets. Most of the patterns we studied are currently inaccessible given the limitations of the experimental methods. Nevertheless, we have highlighted a path to circumvent this issue by introducing cuts on a surface. We have demonstrated, at least for simple enough geometries, that length-minimizing cutting paths tend to follow geodesic trajectories from nearby boundary points. Additionally, with the help of finite thickness simulations, we observed that in situations where the target area distortion is

small compared to the distortion of the uncut domain, it is sometimes necessary to introduce multiple independent cuts in order to buckle into the desired structure.

Finding minimum distortion conformal maps is a problem that has been explored before. Nevertheless this has been done either analytically for simple geometries or numerically for fixed boundary domains. Our main contribution consists of relaxing the fixed boundary constraint in order to reach a specific distortion that provided some experimental limitations. In this paper we explored the paths generated by a greedy algorithm. The procedure we used only focuses on local changes and it is possible that there exist cutting paths that require less cutting to attain the desired distortion.

In the cases where the Gaussian curvature remains sign-fixed, our results confirm an equivalence between minimizing either the Dirichlet energy ω_D or the Chebyshev parameter ω_C. Nonetheless, apparently there are situations where the sign requirement can be violated while both cutting criteria still behave similarly. We realized one of those situations in domains with axial symmetry, like the Gaussian bump, whose swelling minimum is located at the boundary regardless of the change in Gaussian curvature sign.

As previously stated, there could be more sophisticated and complicated cutting approaches. Nevertheless, the method we use is a reasonable candidate when the desired distortion can be obtained without introducing strong boundary layer effects. Another interesting feature that speeds up the computations is that although the method is greedy, it does not need to consider all the accessible boundary but only the portion generated by the cut. This relies on the observation that cuts tend to grow into the surfaces.

During the present work we considered swelling pattern with a disk or simply-connected topology. One possible extension to this could be implemented by adding holes or cone singularities at surface points with high local distortion. Exploring the effect of internal holes might require generalization of the methods used during this work in order to deal with non-disk topologies. This poses a further challenge given that it is not completely understood whether it is possible to extend the minimum distortion theorems used in this paper to systems without a disk topology. Moreover, it is not clear if we can conformally flatten a domain with holes before turning it first into a topological disk. This and other generalizations will be left for future studies.

Conflicts of interest

There are no conflicts of interest to declare.

A Appendices

A.1 Conformal projection of the Gaussian bump

The shape of the Gaussian bump is $\mathbf{R}(r,\theta) = r\hat{\mathbf{r}}(\theta) + z_0 e^{-r^2/(2R^2)}\hat{\mathbf{z}}$, where $\hat{\mathbf{r}}(\theta)$ and $\hat{\mathbf{z}}$ are the unit vectors associated respectively with the (r,z) coordinates of the axis-symmetric surface. The initial metric is:

$$ds^2 = [1 + z'(r)^2]dr^2 + r^2 d\theta^2. \quad (14)$$

We are aiming to rewrite this in terms of a new metric $ds^2 = \Omega(\rho)[d\rho^2 + \rho^2 d\theta^2]$. To do that, we have to apply a change of variables between the (r,θ) and (ρ,θ) planes. To do that, we start with the metric in the (r,θ) plane and change variables to $r = f(\rho)$. Then:

$$ds^2 = [1 + z'(f(\rho))^2]f'(\rho)^2 d\rho^2 + f^2(\rho)d\theta^2. \quad (15)$$

Comparison to the target metric shows that $f(\rho) = \sqrt{\Omega(\rho)}\rho$ (from the $d\theta$ term). The first term then shows that:

$$\left[1 + z'\left(\sqrt{\Omega(\rho)}\rho\right)^2\right]\left[\frac{d}{d\rho}\left(\sqrt{\Omega(\rho)}\rho\right)\right]^2 = \Omega(\rho). \quad (16)$$

Therefore,

$$\frac{d}{d\rho}\left(\sqrt{\Omega(\rho)}\rho\right) = \pm\sqrt{\frac{\Omega(\rho)}{1 + z'\left(\sqrt{\Omega(\rho)}\rho\right)^2}}. \quad (17)$$

Finally,

$$\frac{1}{\sqrt{\Omega(\rho)}}\frac{d}{d\rho}\left(\sqrt{\Omega(\rho)}\rho\right) = \pm\left[1 + z'\left(\sqrt{\Omega(\rho)}\rho\right)^2\right]^{-1/2}. \quad (18)$$

Now, we can put this in a slightly more convenient form using:

$$\frac{d}{d\rho}g^2(\rho) = 2g(\rho)g'(\rho). \quad (19)$$

Therefore,

$$g'(\rho) = \frac{1}{2g(\rho)}\frac{d}{d\rho}g^2(\rho). \quad (20)$$

Using $g(\rho) = \sqrt{\Omega(\rho)}\rho$, we find:

$$\frac{1}{2\Omega(\rho)\rho}\frac{d}{d\rho}(\Omega(\rho)\rho^2) = \pm\left[1 + z'\left(\sqrt{\Omega(\rho)}\rho\right)^2\right]^{-1/2}. \quad (21)$$

Finally, we need to choose the appropriate sign on the right-hand side (the positive sign here) and substitute in $z'(r) = z_0 r/R^2 e^{-r^2/(2R^2)}$. This finally yields:

$$\frac{1}{2\Omega(\rho)\rho}\frac{d}{d\rho}(\Omega(\rho)\rho^2) = \left[1 + \frac{z_0^2\rho^2\Omega(\rho)}{R^4}e^{-\Omega(\rho)\rho^2/R^2}\right]^{-1/2}, \quad (22)$$

which is eqn (12).

A.2 Numerical details and cutting pseudocode

In this appendix we describe some of the details and the pseudocode of the algorithm we used to add cuts on surfaces. The algorithm is designed to split edges connecting one boundary and one interior vertex. The choice of initial boundary vertices can be either user-defined or seeded by any desired method. During this work we seeded the cuts by taking advantage of the symmetry of the uncut surface. We found that, at least for the considered cases, doing this had the advantage of requiring less cutting steps as compared to the case where the cuts were seeded randomly. For example, in the cases where we had azimuthal symmetry, it was observed that the optimal results were obtained by seeding N independent cuts with constant angle spacing. There is not an *a priori* estimate of how many different cuts will be needed. The number of cuts, N, can be tuned to reach the target distortion with the minimum amount of cutting.

Given that the numerical methods we use are only valid for simply-connected cases, the cuts can never separate the triangulations into disconnected pieces. The algorithm exits when it either reaches the desired distortion or runs out valid interior vertices to extend the cuts. In order to solve the non-linear system of eqn (6) we use a modified version of the Powell dogleg algorithm suitable for sparse systems of equations.[25] This method requires a linear system of equations solver. We use the PARDISO library which is also suitable for sparse systems.[26] To estimate the error introduced by our discrete flattenings, we used the unitless convex energy reported by Springborn *et al.*[16] given that the process of minimizing the convex energy is equivalent to solving the non-linear system 6. In our case, we computed the magnitude of the gradient of this energy and obtained values in the range of 10^{-14}–10^{-12}. Finally, the pseudocode of our greedy algorithm is the following:

Algorithm 1: Discrete conformal flattening with a desired distortion

Input: *Surface triangulation $T = (V, E, F)$, a conformal flattening (a discrete conformal mapping of T on $\mathbb{R}^2$), distortion given by $\omega_C^{current}$, a target distortion given by either ω_C^{target} (ω_D^{target} or any other measures can be used instead), a set containing N (number of independent cuts) subsets $V_{seed} = \{\{v_{seed}\}\}$. Each subset initially only contains a single vertex which act as independent cutting seeds.*

Output: *A discrete conformal flattening with $\omega_C \leq \omega_C^{target}$.*

while $\omega_C^{current} \geq \omega_C^{target}$ **do**

1. *Define the empty set $V_{optimal} = \{\}$.*
2. **forall** *subset $\{v_{seed}\}_k$ in V_{seed}* **do**
   1. **forall** *Vertex v_i in $\{v_{seed}\}_k$* **do**
      1. *Find the set of internal vertices V_{int} connected to the boundary vertex v_i;*
      2. **if** *V_{int} is empty* **then go to** 6;
      3. **forall** *vertices v_j in V_{int}* **do**
         1. *Cut along the internal edge $[v_i, v_j]$;*
         2. *Compute a discrete conformal flattening consistent with the modified boundary;*
         3. *Compute the distortion $\omega_C^{modified}$ of the modified triangulation;*
         4. **if** *$\omega_C^{modified} < \omega_C^{current}$* **then**
            1. *$\omega_C^{current} = \omega_C^{modified}$;*
            2. *Define $v_{optimal} = v_j$ and $e_{optimal} = [v_i, v_j]$ as the optimal vertex and edge respectively;*
         5. *Undo the cut along the edge $[v_i, v_j]$;*
      4. *Cut along $e_{optimal}$ and make it a permanent cut.*
      5. *Add the boundary vertex $v_{optimal}$ to the sets $\{v_{seed}\}_k$ and $V_{optimal}$.*
      6. **continue**
3. **if** *$V_{optimal}$ is empty* **then exit**;

Acknowledgements

We acknowledge valuable conversations with K. Crane and E. Vouga. This work was funded by the National Science Foundation under grant DMR-1507377.

References

1 S. Tibbits, *Archit. Des.*, 2014, **84**, 116–121.
2 J. Kim, J. A. Hanna, M. Byun, C. D. Santangelo and R. C. Hayward, *Science*, 2012, **335**, 1201–1205.
3 Y. Klein, E. Efrati and E. Sharon, *Science*, 2007, **315**, 1116–1120.
4 J.-H. Na, N. P. Bende, J. Bae, C. D. Santangelo and R. C. Hayward, *Soft Matter*, 2016, **12**, 4985–4990.
5 A. S. Gladman, E. A. Matsumoto, R. G. Nuzzo, L. Mahadevan and J. A. Lewis, *Nat. Mater.*, 2016, **15**, 413.
6 T. J. White and D. J. Broer, *Nat. Mater.*, 2015, **14**, 1087.
7 T. H. Ware, M. E. McConney, J. J. Wie, V. P. Tondiglia and T. J. White, *Science*, 2015, **347**, 982–984.
8 H. Aharoni, Y. Xia, X. Zhang, R. D. Kamien and S. Yang, *Proc. Natl. Acad. Sci. U. S. A.*, 2018, **115**, 7206–7211.
9 D. R. Espeso, A. Carpio and B. Einarsson, *Phys. Rev. E: Stat., Nonlinear, Soft Matter Phys.*, 2015, **91**, 022710.
10 H. Liang and L. Mahadevan, *Proc. Natl. Acad. Sci. U. S. A.*, 2011, **108**, 5516–5521.
11 Y. Pan, I. Heemskerk, C. Ibar, B. I. Shraiman and K. D. Irvine, *Proc. Natl. Acad. Sci. U. S. A.*, 2016, **113**, E6974–E6983.
12 E. Efrati, E. Sharon and R. Kupferman, *J. Mech. Phys. Solids*, 2009, **57**, 762–775.
13 N. P. Bende, R. C. Hayward and C. D. Santangelo, *Soft Matter*, 2014, **10**, 6382–6386.
14 P. Henrici, *Applied and Computational Complex Analysis*, John Wiley & Sons, 1993, vol. 3, pp. 287–294.
15 W. Zeng, F. Luo, S.-T. Yau and X. D. Gu, IMA International Conference on Mathematics of Surfaces, 2009, pp. 391–408.
16 B. Springborn, P. Schröder and U. Pinkall, *ACM Trans. Graph.*, 2008, **27**, 77:1–77:11.
17 P. L. Chebyshev, *Oeuvres de P. L. Tchebychef*, Chelsea Publishing Company, New York, 1962, pp. 233–236 and 239–247.
18 D. Gravé, *J. Reine Angew. Math.*, 1911, **140**, 247–251.
19 J. Milnor, *Am. Math. Mon.*, 1969, **76**, 1101–1112.
20 N. Sharp and K. Crane, *ACM Trans. Graph.*, 2018, **37**, 156.
21 A. I. Bobenko and B. A. Springborn, *Discrete Comput. Geom.*, 2007, **38**, 740–756.
22 H. S. Seung and D. R. Nelson, *Phys. Rev. A: At., Mol., Opt. Phys.*, 1988, **38**, 1005–1018.
23 B. G.-g. Chen and C. D. Santangelo, *Phys. Rev. E: Stat., Nonlinear, Soft Matter Phys.*, 2010, **82**, 056601.
24 V. Vitelli and D. R. Nelson, *Phys. Rev. E: Stat., Nonlinear, Soft Matter Phys.*, 2004, **70**, 051105.
25 HSL, *A collection of Fortran codes for large scale scientific computation*, 2013, http://www.hsl.rl.ac.uk.
26 O. Schenk and K. Gärtner, *Future Gener. Comput. Syst.*, 2004, **20**, 475–487.